Chaotic mixing of immiscible impurities in a two-dimensional flow

T. H. Solomon*, S. Tomas and J. L. Warner

Department of Physics, Bucknell University, Lewisburg, PA 17837

(October 26, 1997)

Abstract

Experiments compare the chaotic mixing of miscible and immiscible impurities in a two-dimensional flow composed of a chain of alternating vortices. Periodic time-dependence is imposed on the system by sloshing the fluid slowly across the stationary vortices, mimicking the even oscillatory instability of Rayleigh-Bénard convection. The transport of a miscible impurity is diffusive with an enhanced diffusion coefficient D^* that depends on the size of "lobes" which are, in turn, dependent on the oscillation amplitude. The lobes play an important role in the transport of *immiscible* impurities as well. In this case, the impurity is broken into a distribution of droplets, whose areas determine the nature of the transport. If the characteristic long-term droplet areas are appreciably smaller than the lobe areas, then there is long-range transport with D^* equal to that for the miscible case with the same flow conditions. If the droplet areas remain larger than the lobe areas, then there is no long-range transport.

47.52.+j, 66.10.-x, 51.20.+d, 92.10.Lq

I. INTRODUCTION

Passive tracers moving in time-dependent velocity fields often follow chaotic paths, in the sense that nearby trajectories separate rougly exponentially in time ("sensitive dependence on initial conditions"). This process, referred to as *chaotic advection* [1], can occur even if the time dependence is periodic. Formally, for a two-dimensional fluid flow, the equations integrated to determine the trajectories are Hamilton's equations of motion, and the particle paths can be described as phase space trajectories of a chaotic system [2]. As a result, analytical tools developed to study Hamiltonian chaos can be applied simply to the study of chaotic advection.

The mixing and transport of a blob of a miscible (soluble) impurity can be influenced substantially by chaotic advection [3], since each molecule can be treated as an independent tracer. If the tracer trajectories are chaotic, then sensitive dependence on initial conditions can result in rapid spreading of the blob. Several previous studies have investigated the signatures of Hamiltonian chaos in the mixing of miscible impurities [4,5], along with enhancements in long-range mixing due to chaotic advection [6]. Less is known about the mixing of *immiscible* impurities (such as oil in water), due to the complicating effects of surface tension, which results in length-dependent attractive forces between impurity molecules. Clearly, the simple Hamiltonian formalism typically used to describe chaotic mixing has to be modified for the mixing of immiscible impurities, since the phase space trajectories are no longer independent of each other.

In this article, we describe experiments comparing and contrasting long-range, enhanced, chaotic mixing of miscible and immiscible impurities in a two-dimensional, time-periodic flow [7]. Magnetohydrodynamic forcing is used to generate a chain of alternating vortices in a thin layer of water. Time dependence is imposed by oscillating the fluid slowly back and forth across the cell. With this arrangement, which mimicks the "even" oscillatory instability of Rayleigh-Bénard convection [6,8,9], independent control is achieved for the flow velocities, oscillation amplitudes and oscillation frequencies. The result is an experimental

arrangement that allows for more precise measurements of mixing phenomena than were achieved in previous experiments [6]. Experiments are performed with both a molecular dye (uranine) and an oil that floats on the surface of the fluid.

For the mixing of a miscible impurity, the transport is governed by "lobes" [10,11] that exchange impurity between one vortex and the next. For immiscible impurities, the process is characterized by the break-up of oil droplets into a steady-state distribution. Long-range transport is found to be inhibited if the long-term characteristic droplet area is larger than the area of lobes for miscible mixing with the same flow conditions. On the other hand, if the droplets are broken down to sizes appreciably smaller than the lobes, they behave as individual passive tracers, and the transport rates from the miscible case are recovered.

In Section II, we discuss theories and previous experimental studies of chaotic mixing. The experimental apparatus and techniques are explained in Section III. The results of the experiments are presented in Section IV, and are summarized in Section V.

II. BACKGROUND

For a motionless fluid, transport of a miscible impurity is governed by molecular diffusion [12], caused by random Brownian motion of individual impurity molecules. In the presence of a fluid flow, the transport is modified by advection of the impurity with the flow. If the advection is chaotic, then the trajectories of individual molecules can be similar to Brownian motion on a macroscopic scale: even though the trajectories are deterministic, they undergo what appears to be a "random walk." It is therefore reasonable to analyze transport in a fluid flow as an enhanced diffusion process.

Quantitatively, diffusion processes are analyzed by monitoring the growth of the variance $\langle x^2 \rangle$ with time. Often, this growth can be described as a power law: $\langle x^2 \rangle \sim t^\gamma$. If $\gamma \neq 1$, then the process is called *anomalous diffusion* [13,14]. If $\gamma = 1$, then the process is referred to as *normal diffusion*. Specifically, for normal diffusion, the variance $\langle x^2 \rangle = 2D^* t$, where D^* is the *enhanced diffusion coefficient*.

Earlier experiments measured enhanced diffusion for passive (miscible) transport in quasi-two-dimensional, time-independent [15] and time-periodic [6,8] Rayleigh-Bénard (thermal) convection. A picture of the (idealized) velocity field for this flow is shown in Fig. 1. Although Rayleigh-Bénard convection is three-dimensional, a cross section of the flow shows a two-dimensional velocity field composed of a chain of alternating vortices. If the Rayleigh number R (dimensionless forcing, proportional to the imposed temperature difference) is sufficiently small, the velocity field is time-independent. For larger R, the flow can be oscillatory, with the vortices oscillating back and forth periodically [16]. The streamfunction for the flow in Fig. 1 is given by $\psi = \frac{A}{k}\sin(kx)W(y)$, where A and k are the amplitude and wavenumber, and $W(y)$ is a function the accounts for the no-slip condition at the top and bottom boundaries (see Ref. [17] for more details). The x- and y-components of the velocity can be obtained from this streamfunction with Hamilton's equations $\dot{x} = \frac{\partial \psi}{\partial y}$ and $\dot{y} = -\frac{\partial \psi}{\partial x}$.

For the time-periodic flow, comparisons were made in the earlier experiments [6,8] between the experimental observations and numerical simulations of chaotic advection in a model of the flow. Repeated stretching and folding of tendrils of the impurity were observed in both cases, indicative that the transport in the system was, in fact, controlled by chaotic advection. Measurements of the enhanced diffusion coefficients showed rough agreement with the numerical model, although detailed comparisons were complicated by deviations of the experimental flow from the ideal case.

The problem of enhanced diffusion in two-dimensional, time-periodic flows has been addressed theoretically [9–11] by considering "lobes" formed from the intersection of stable and unstable manifolds of the hyperbolic fixed points. These lobes form "turnstiles" [2] that exchange fluid between neighboring vortices. Recent experiments [7] tested these theories and demonstrated that enhanced diffusion coefficients are determined in these systems purely by the geometry of the lobes.

As for immiscible fluids, most of the previous studies have investigated the stretching and breakup of a single drop in low Reynolds number flows [18]. The break-up of immiscible impurities due to chaotic advection was studied recently by Muzzio, Tjahjadi and Ottino

[19] in an oscillatory, journal-bearing flow. These experiments found the steady-state droplet size distributions to approach a self-similar relation. We are unaware of any previous studies of long-range, chaotic transport of immiscible impurities.

III. EXPERIMENTAL APPARATUS AND TECHNIQUES

The apparatus for the experiment is shown in Fig. 2. A Plexiglas box is constructed with a raised central portion, above which the vortex chain is generated. A salt water solution fills the bottom of the box to a height of 0.20 cm above the central region. The flow for these experiments is generated by a magnetohydrodynamic technique [20]: a 10 mA current passing length-wise through the cell interacts with an alternating magnetic field, which is produced by a linear array of 14 Nd-Fe-Bo magnets below the fluid layer (Fig. 2b). There are no fluid flows generated by longitudinal electrical forces since the fluid is electrically neutral. In terms of the electrical current $\vec{I}$, bulk motion of positive ions in the direction of $\vec{I}$ is balanced by opposite motion of negative ions. Magnetic forces, however, are significant, since both positive and negative ions experience forcing in the same direction (perpendicular to both $\vec{I}$ and to the magnetic field $\vec{B}$. [21] The Lorentz magnetic force between the current and the alternating magnetic field ($\vec{F}_{mag} = \vec{I} \times \vec{B}$) results in alternating horizontal forcing of the fluid. The result is a chain of vortices with alternating signs. The magnets are each 1.91 cm in diameter, and there is no space between adjacent magnets, so the center-to-center vortex spacing is 1.91 cm.

Two Plexiglas sidewalls bound the vortex chain on either side, giving the region of interest overall dimensions 3.8 cm x 26.7 cm with a fluid thickness 0.20 cm. (The width of 3.8 cm is twice the magnet diameter and the center-to-center vortex spacing, giving the vortices an aspect ratio of 2.) A double-step tab [22] is milled into the bottom of the side walls to pin the interface properly (Fig. 2c). Since the oil is floating on the surface of the water, it is absolutely critical that the water-air interface be level in the region of interest. Furthermore, the oil cannot touch the side walls, since it tends to adhere to Plexiglas. The fluid in the

central region is pinned to the corner of the upper step and slopes down slightly above the bottom step. With this technique, the fluid is level in the central region of the apparatus, where the vortex chain is. The upper step has a height of 0.05 cm, compared to 0.20 cm for the lower step; consequently, the fluid layer is extremely thin above the lower step, inhibiting any appreciable flow from penetrating into the step region.

For small currents, the velocity field is time-independent. Increasing the current results in an instability to time-periodic vortex oscillations. This instability, however, is very sensitive to small imperfections in the apparatus. Furthermore, with this particular instability, there is no way to control the amplitude of the oscillations without changing the fluid velocities as well. For these reasons, we use a different technique to impose time dependence on the flow. We use a driving current I = 10 mA that leaves the flow comfortably within the time-independent regime, with typical velocities ranging up to $\sim$ 0.7 cm/s. Time dependence is imposed by oscillating the fluid across the stationary velocity field, mimicking the oscillatory instability. A small plunger oscillates vertically in a fluid reservoir at one end of the cell. The period of the oscillation (19 s) is chosen to be substantially longer than the viscous diffusion time for a 0.20 cm thick water layer ($\sim$ 4 s), ensuring that the oscillations do not perturb the time-independent velocity field.

For experiments on miscible transport, sodium fluorescein (uranine) dye is used as the impurity, mixed with trace amounts of ethanol to make the dye neutrally-buoyant. Experiments on immiscible mixing are conducted with a fluorescent oil (APD oil dye P/N 801) with a viscosity 15 cp. An important property of the dye is its surface tension when in contact with water and with air. This surface tension, which plays a significant role in the droplet breakup process, depends critically on the level of contamination in the system (e.g., residual soap, grease, etc). In these experiments we take advantage of this property to vary the surface tension from run to run. Specifically, the surface tension is controlled by the addition of small traces of RBS soap solution (which is also used to clean the cell between runs).

Characterization of the surface tension is achieved indirectly by measuring the resiliency

of droplets. Specifically, the time for a droplet with area 5 cm^2 to relax from an aspect ratio of 4 to an aspect ratio of 2 is measured. Studies by Tjahadi, Ottino and Stone [23] have shown that for *suspended* droplets in a three-dimensional system, this relaxation time is correlated very well with the surface tension, although the problem is still being studied for the two-dimensional case with oil floating on water [24]. In the experiments reported in this article, three different resiliencies are used with relaxation times $\tau = 3$, 1.5 and 0.5 s (small, medium and large resiliency, respectively).

Both uranine and the APD oil are fluorescent, so the transport is visualized with black light illumination. The intensity of the fluorescing light is proportional to the impurity concentration, assuming the concentration isn't too high. (For large uranine concentrations, the signal saturates.)

Each experimental run is prepared by injecting the impurity into the central vortex in the absence of any plunger oscillations. For miscible studies, the dye is allowed to spread to cover the complete vortex, at which time the plunger is turned on. In all the experiments shown here, time $t = 0$ corresponds to the moment at which the oscillations are initiated. For runs with oil, the oil is allowed to spread roughly to its full extent before the plunger is turned on. For this reason, many of the oil runs begin with oil in several vortices.

The fluid flow is not rigorously two-dimensional in these studies. There is a very small, secondary, three-dimensional flow within the vortices [15] which is due to Ekman pumping [25]. This flow is an order of magnitude weaker than the primary vortex flow, and circulates between the edges and centers of the vortices. As a result, mixing *within* the vortices is enhanced, and Kolmogorov-Arnold-Moser (KAM) invariant surfaces are ineffective at blocking mixing over long time-scales. However, the secondary flow does not contribute to transport from one vortex to another, which is governed predominately by chaotic advection.

IV. RESULTS

A. Miscible impurities

The transport of uranine dye is measured for three different oscillation amplitudes $b = 0.06$, 0.12 and 0.24, where b is the dimensionless amplitude b = (oscillation amplitude)/(vortex width). A sequence showing the transport behavior for $b = 0.12$ is shown in Fig. 3. Three lobes are visible in the second image, two carrying dye from the central vortex to its neighbors, and one carrying clear fluid back into the central vortex. As time progresses, the lobes are stretched into long tendrils and folded back on themselves repeatedly, a classic signature of chaotic phenomena. KAM barriers are visible early in the run as "holes" in the middle of the vortices, although those holes fill in after a few minutes due to a combination of Ekman pumping (described in Section II) and molecular diffusion. The secondary Ekman flow can be seen in Fig. 3 by the fact that a hole opens up in the center vortex, due to the secondary flow which carries clear fluid up through the center.

As discussed in a previous paper [7], measurement of the areas of the lobes from these images can be used to predict the enhanced diffusion coefficients D^*. Alternately, D^* can be determined directly by measuring the variance $\langle x^2 \rangle$ of the dye distribution and plotting $\langle x^2 \rangle$ as a function of time. Each dye image (after the background is subtracted) is summed vertically to obtain a one-dimensional concentration profile $C(x)$. The profile is then smoothed horizontally (boxcar averaging) to reduce variations caused by tendril structure within the vortices (Fig. 4) [26]. The smoothed concentration profiles are then fitted to Gaussians, from which $\langle x^2 \rangle$ can be determined.

A plot of $\langle x^2(t) \rangle$ for the $b = 0.12$ data from Fig. 4 is shown in Fig. 5, along with plots from experiments with b = 0.06 and 0.24. The solid lines show the growth in $\langle x^2 \rangle$ expected from the lobe analysis. (For reference, the lobes are measured to have areas $l = 0.28$ cm^2, 0.58 cm^2 and 1.09 cm^2 for $b = 0.06$, 0.12 and 0.24, respectively.) The enhanced diffusion coefficient D^* is one-half the slope of these plots: $D^* = 0.007$ cm^2/s, 0.015 cm^2/s and 0.029

cm^2/s ($\pm$ 0.001 cm^2/s) for $b = 0.06$, 0.12 and 0.24, respectively. (A clear scaling region is not observed for the $b = 0.24$ case; however, the behavior is consistent with the prediction based on the lobe analysis.)

B. Immiscible mixing, b = 0.12

Transport of an immiscible impurity is characterized in the short term by the formation (or partial formation) of lobes at the corners of the inner vortex (Fig. 6). In contrast to the miscible case, though, surface tension significantly affects the stretching of these lobes into tendrils. If the drop resiliency is large (Fig. 6c), the lobes are often pulled back by surface tension into the central vortex, inhibiting long-range transport. Small resiliency droplets are stretched into tendrils (Fig. 6a), but unlike those for miscible impurites, these tendrils cannot be stretched indefinitely. Rather, a capillary instablity causes the tendril to break, as seen in the the top 3 images of Fig. 6(a).

After the short-term break-up of the oil droplets, long-range transport is (or is not) achieved by the advection (or lack thereof) of the droplets as individual tracers. In Fig. 6(a), the small droplets undergo the same seemingly "random walk" between vortices as seen in earlier simulations [6,8] and experiments [14] of passive tracer transport. The result is a spreading of the overall impurity distribution.

Quantitatively, transport for the immiscible case is analyzed in the same manner as for miscible experiments, as described in the previous section. Each image of the fluorescing oil is summed vertically to obtain a concentration profile, which is then smoothed and fit to a Gaussian (Fig. 7). The concentration profiles for the oil are substantially more choppy than those for the miscible case, due to the discrete nature of the oil droplets. Furthermore, the advection of an individual droplet off the edge of the viewable area (or back in) can cause a jump in the variance. Consequently, plots of $\langle x^2(t) \rangle$ for oil runs are somewhat noisy (Fig. 8). Nevertheless, the overall trends are still clear.

In Fig. 8, $\langle x^2(t) \rangle$ is plotted for the oil runs shown in Figs. 6(a) and (b), along with $\langle x^2(t) \rangle$

for the miscible experiment from Fig. 3 (also with $b = 0.12$). Transport for oil with small resiliency (τ =3.0 s), denoted by the squares, is characterized by the same effective diffusion coefficient D^* as for the miscible case, seen by the fact that $\langle x^2(t) \rangle$ grows with the same slope for the two cases. Transport is more restricted for oil with intermediate resilience (τ =1.5 s), denoted by the triangles, as indicated by the slower growth in the variance. Experiments with large droplet resiliency (τ = 0.5 s, Fig. 6c) are not shown on this graph. These runs are characterized by a variance that remains constant, indicative of no long-range transport ($D^* = 0$) [27].

There are currently no theories that address completely the chaotic transport of immiscible impurities. We interpret the results in these experiments here with a simplified, phenomenological approach that considers the size distributions for the oil droplets. The experiments with small resiliency (large τ) are characterized by the breakup of the oil into very small droplets. Theoretically, if the droplets are small enough, they should behave as ideal, passive tracers [28]. In this regime, which we will refer to as the *tracer regime*, the transport should proceed with an enhanced diffusion coefficient D^* equal to that for the miscible case. On the other hand, if the flow is unable to break down the droplets small enough, due either to large drop resiliency (small τ) or to a weak flow, then surface tension effects should inhibit long-range transport (*blob regime*). The question then becomes: how small is small enough? Considering the importance of lobes in the transport process, it is natural to compare the droplet sizes to the lobe size. In the following discussion, the droplet areas are scaled by the area of lobes measured for miscible transport with the same flow conditions; the non-dimensional area is then given by $\Gamma = A/l$, where A is the droplet area and l is the lobe area.

The analysis proceeds as follows: each image is binarized with an intensity threshold chosen such that only the pixels in the image occupied by oil have intensities exceeding the threshold. Blob analysis is then done to identify the separate clusters of pixels and determine their areas [29]. Histograms of these areas are quite choppy, since there are typically less than a couple hundred droplets, even after the break-up process is complete. Furthermore, a

histogram itself is not very informative, since it is not the *number* of droplets of a particular size that is critical for transport but rather *what fraction* of oil is contained in drops with certain sizes.

To determine a characteristic droplet size, the histograms are weighted by the droplet areas and integrated to determine fraction distributions $f(\Gamma) = \frac{1}{N}\int_0^\Gamma \Gamma' p(\Gamma') d\Gamma'$ where $p(\Gamma)$ is the probability distribution function for droplets with non-dimensional size Γ and the normalization constant is given by $N = \int_0^\infty \Gamma' p(\Gamma') d\Gamma'$. The fraction distribution $f(\Gamma)$ is a measure of the fraction of the oil in the system that is contained in droplets with non-dimensional area less than Γ. A plot of $f(\Gamma)$ is shown in Fig. 9 for the experiment of Fig. 6(a) (small resiliency, $\tau = 3.0$ s). The characteristic droplet size Γ_c is defined such that $f(\Gamma_c) = 0.5$, i.e., half of the oil is contained in droplets with non-dimensional area less than Γ_c. A plot of $\Gamma_c(t)$ is shown in Fig. 10 for the experiments shown in Fig. 6.

Comparing plots of the characteristic droplet size $\Gamma_c(t)$ (Fig. 10) and the variance $\langle x^2(t)\rangle$ (Fig. 8) give an indication of how small the droplets need to be to behave as passive tracers from a mixing perspective. For the large resiliency case ($\tau = 0.5$s, Fig. 10b), $\Gamma_c \to 2.0$ in the long time limit, clearly too large for any appreciable long-range transport. On the other hand, Γ_c approaches 0.17 in experiments with resiliency time $\tau = 3.0$ s, which display long-range transport equivalent to the miscible case (see Figs. 6(a) and 8). A cross-over between the tracer and blob regimes can be seen in the data of Fig. 6(b) with $\tau = 1.5$ s. This run displays long-range transport, but with a significantly reduced D^*. For this case, Γ_c approaches 0.31 in the long time limit.

The data here seem to indicate that, for dimensionless oscillation amplitude b = 0.12, the droplets need to be broken down to a characteristic area less than approximately a quarter of the lobe area to behave as passive tracers and recover the enhanced transport of the miscible case. The following sections explore these ideas further with different oscillation amplitudes to see if this behavior is independent of the flow conditions.

C. Immiscible mixing, $b = 0.24$ and 0.06

In general, increasing the oscillation amplitude b results in more significant oil breakup and smaller resulting droplet areas A. Furthermore, the lobe area l is larger for larger b. The result is substantially smaller non-dimensional droplet sizes $\Gamma = A/l$ for large b. Consequently, if the interpretation of the results from the previous section is valid, the tracer regime should be easily achieved for $b = 0.24$, and should be very difficult to achieve for $b = 0.06$.

A sequence showing the transport of small resiliency oil ($\tau = 3.0$ s) for b = 0.24 is shown in Fig. 11(a). In this case, the droplets are absolutely *shattered*, as can be seen in Fig. 12(a), with the characteristic droplet size Γ_c dropping to 0.06 in the first minute. As expected, the variance $\langle x^2 \rangle$ for this sequence (Fig. 12(b), triangles) grows almost identically to that for a miscible dye in the same flow (upper, solid curve).

An oil with large resiliency ($\tau = 0.5$ s) also displays good long-range transport for $b = 0.24$, although it takes longer for the transport to get going. As can be seen in Fig. 11(b), the oil doesn't start to break up appreciably until 180 s after initiation of the time dependence. Quantitatively, it takes approximately 200 s for the characteristic droplet area Γ_c to drop below 1, and 400 s for Γ_c to drop below 1/3 (Fig. 12a). This is reflected in the variance $\langle x^2 \rangle$, which does not grow appreciably until after 200 s. After this point, however, $\langle x^2 \rangle$ grows with a slope equal to that for the miscible case. The long-term Γ_c for this experiment is approximately 0.22, consistent with the results from the previous section that indicate that the tracer regime is achieved if $\Gamma_c \lesssim 1/4$.

For experiments with oscillation amplitude $b = 0.06$, the decrease in the lobe size (due to the small oscillation amplitude), coupled with the larger steady state droplet areas makes it difficult to get a situation with $\Gamma_c < 1/4$. Runs with $\tau = 1.5$ and 0.5 s all have $\Gamma_c > 1$ in the long time limit, and there is no long-range transport, consistent with identification of these runs as being in the blob regime. Even with small drop resiliency ($\tau = 3.0$ s), the transport is significantly reduced as compared with the miscible case, as seen in Fig. 13.

The variance (after a brief transient period) is constant up through 1000 s, after which it increases very slowly (Fig. 13b). This is consistent with the fact that the droplet breakup process (Fig. 13c) is extremely slow in this case, with $\Gamma_c > 1$ for the first 500 s and levelling off at 0.64 after 1300 s.

To test further the idea that the droplet sizes are the primary factor in determining the transport behavior, another experiment was done with small oscillation amplitude $b = 0.06$ and droplet resiliency $\tau = 3.0$ s, but this time, the oil was broken up manually by stirring it violently with a small dowel rod (Fig. 14). The resulting characteristic droplet size Γ_c is 0.16. Consistent with the previous analysis, the variance $\langle x^2 \rangle$ grows with a slope equal to that for the miscible case with $b = 0.06$ (Fig. 14b), indicating tracer-like transport. (The large initial value for $\langle x^2 \rangle$ is due to the fact that the oil was sprayed over several vortices during the manual break-up process.) It is also noteworthy here that Γ_c increases in the long-time limit as small droplets congeal to form larger ones. This aggregation process is not significant, though, until there has already been appreciable long-range transport.

V. DISCUSSION AND SUMMARY

Despite the substantial complication introduced by surface tension effects, we have shown that chaotic mixing of immiscible impurities can still be interpreted using the standard, Hamiltonian tools of chaotic advection. The process is characterized by the break-up of the impurities into smaller droplets whose sizes determine the nature of the transport. A characteristic non-dimensional droplet area Γ_c (normalized by the lobe area) is defined as a parameter to denote the different mixing regimes, independent of the flow conditions and the impurity surface tensions.

A *tracer regime* has been identified in which transport of immiscible impurities proceeds with the same enhanced diffusion coefficient D^* as for the miscible case. The condition for this tracer regime appears to be that the droplet areas be appreciably smaller than the lobes (determined from experiments with *miscible* impurities). Specifically, tracer-like transport

is observed in all cases where the non-dimensional characteristic droplet area Γ_c is less than 1/4. On the other hand, a *blob regime* is found if the flow is not able to break up the drops small enough. In this case, where the characteristic droplet areas are *larger* than lobe areas ($\Gamma_c > 1$) in the long-time limit, there is no appreciable long-range transport at all. An intermediate regime has been observed for Γ_c ranging from approximately 0.3 to 0.7. In this case, there *is* long-range transport, but with a reduced D^*.

Experiments are currently in progress to address the droplet breakup process itself in more detail, along with the aggregation phenomena seen in the bottom image of Fig. 14(a). Presumably, different flows should result in different steady-state droplet distributions, and a understanding of these distributions is needed for a complete theoretical description of the process.

It is our hope that these experiments will stimulate more complete theoretical studies of transport phenonema for immiscible impurities. In particular, more studies are needed to understand the break-up process better and to relate this process to long-range transport. Furthermore, the role of surface tension has to be incorporated in more detail into any complete model of immiscible transport.

ACKNOWLEDGMENTS

We are pleased to acknowledge the assistance of Dave Vayda and Steve Brafa in the design and construction of the apparatus, along with M.F. Schatz, who suggested the double-step sidewalls. Support for S. Tomas and J.L. Warner was provided by NSF REU through Grant No. PHY-9423936. The experiments were also supported by a Cottrell College Science Award of Research Corporation (Grant No. CC4002).

REFERENCES

* Electronic mail: tsolomon@bucknell.edu

[1] H. Aref, "Stirring by chaotic advection," J. Fluid Mech. **143**, 1 (1984).

[2] R.S. MacKay, J.D. Meiss, and I.C. Percival, "Transport in Hamiltonian systems," Physica (Amsterdam) **13D**, 55 (1984).

[3] J.M. Ottino, *The kinematics of mixing: stretching, chaos, and transport* (Cambridge U. P., Cambridge, 1989).

[4] D.V. Khakhar, H. Rising, and J.M. Ottino, "An analysis of chaotic mixing in two chaotic flows," J. Fluid Mech. **172**, 419 (1986).

[5] J. Chaiken, R. Chevray, M. Tabor and W.M. Tam, "Experimental study of Lagrangian turbulence in Stokes flow," Proc. R. Soc. London Ser. A. **408**, 165 (1987).

[6] T.H. Solomon and J.P. Gollub, "Chaotic particle transport in time-dependent Rayleigh-Bénard convection," Phys. Rev. A **38**, 6280 (1988).

[7] T.H. Solomon, S. Tomas and J.L. Warner, "Role of lobes in chaotic mixing of miscible and immiscible impurities," Phys. Rev. Lett. **77**, 2682 (1996).

[8] J.P. Gollub and T.H. Solomon, "Comples particle trajectories and transport in stationary and periodic convective flows," Physica Scripta **40**, 430 (1989).

[9] R. Camassa and S. Wiggins, "Chaotic advection in a Rayleigh-Bénard flow," Phys. Rev. A **43**, 774 (1991).

[10] V. Rom-Kedar and S. Wiggins, "Transport in two-dimensional maps: concepts, examples, and a comparison of the theory of Rom-Kedar and Wiggins with the Markov Model of MacKay, Meiss, Ott, and Percival," Physica (Amsterdam) **51D**, 248 (1991).

[11] S. Wiggins, *Chaotic Transport in Dynamical Systems* (Springer-Verlag, New York, 1992).

[12] E.L. Cussler, *Diffusion: Mass Transfer in Fluid Systems* (Cambridge University PRess, Cambridge, 1984).

[13] See, e.g., W. Young, A. Pumir and Y. Pomeau, "Anomalous diffusion of tracers in convection rolls," Phys. Fluids A **1**, 462 (1989); O. Cardoso and P. Tabeling, "Anomalous diffusion in a linear system of vortices," Eur. J. Mech. B/Fluids **8**, 459 (1989); B.D. Hughes, M.F. Shlesinger and E.W. Montroll, "Random walks with self-similar clusters," Proc. Natl. Acad. Sci. USA **78**, 3287 (1981); M.F. Shlesinger, G.M. Zaslavsky and J. Klafter, "Strange kinetics," Nature **363**, 31 (1993).

[14] T.H. Solomon, E.R. Weeks and H.L. Swinney, "Observation of anomalous diffusion and Lévy flights in a two-dimensional rotating flow," Phys. Rev. Lett. **71**, 3975 (1993); T.H. Solomon, E.R. Weeks and H.L. Swinney, "Chaotic advection in a two-dimensional flow: Lévy flights and anomalous diffusion," Physica D **76**, 70 (1994).

[15] T.H. Solomon and J.P. Gollub, "Passive transport in steady Rayleigh-Bénard convection," Phys. Fluids **31**, 1372 (1988).

[16] E.W. Bolton, F.H. Busse, and R.M. Clever, "Oscillatory instabilities of convection rolls at intermediate Prandtl numbers," J. Fluid Mech. **164**, 469 (1986).

[17] S. Chandrasekhar, *Hydrodynamic and Hydromagnetic Stability* (Dover, New York, 1961).

[18] G.I. Taylor, "The formation of emulsions in definable fields of flow," Proc. R. Soc. Lond. A **146**, 501 (1934); F.D. Rumscheidt and S.G. Mason, "Particle motions in sheared suspensions. XII Deformation and burst of fluid drops in shear and hyperbolic flow," J. Colloid Sci **16**, 238 (1961); B.J. Bentley and L.G. Leal, "An experimental investigation of drop deformation and breakup in steady two-dimensional linear flows," J. Fluid Mech. **167**, 241 (1986); H.A. Stone and L.G. Leal, "Relaxation and breakup of an initially extended drop in an otherwise quiescent fluid," J. Fluid Mech. **198**, 399 (1989); H.A. Stone and L.G. Leal, "The influence of initial deformation on drop breakup in subcritical

time-dependent flows at low Reynolds number," J. Fluid Mech. **206**, 223 (1989).

[19] F.J. Muzzio, M. Tjahjadi, and J.M. Ottino, "Self-similar drop size distributions produced by breakup in chaotic flows," Phys. Rev. Lett. **67**, 54 (1991); M. Tjahjadi and J.M. Ottino, "Stretching and breakup of droplets in chaotic flows," J. Fluid Mech. **232**, 191 (1991).

[20] H. Willaime, O. Cardoso, and P. Tabeling, "Spatiotemporal intermittency in lines of vortices," Phys. Rev. E **48**, 288 (1993).

[21] The magnetic force on a moving ion is given by $\vec{F}_{ion} = q\vec{v}x\vec{B}$. For a DC current, $\vec{v}$ for the positive ($q > 0$) ions is in the opposite direction as for negative ($q < 0$) ions, so $\vec{F}_{ion}$ points in the same direction for all ions, resulting in bulk fluid motion.

[22] M.F. Schatz, S.J. VanHook, W.D. McCormick, J.B. Swift, and H.L. Swinney, "Onset of surface-tension-driven Bénard convection," Phys. Rev. Lett. **75**, 1938 (1995).

[23] M. Tjahjadi, J.M. Ottino, and H.A. Stone, "Estimating interfacial tension via relaxation of drop shapes and filament breakup," AIChE J. **40**, 385 (1994).

[24] P. DeRoussel and J. Ottino (private communication).

[25] D.J. Tritton, *Physical Fluid Dynamics* (Clarendon Press, Oxford, 1988); T.H. Solomon, "Transport and boundary layers in Rayleigh-Bénard convection," PhD Dissertation (Univ. Pennsylvania, 1990).

[26] The area under the profiles is reduced early in the run in Fig. 4, due to saturation of the dye. (The initial concentration in the center vortex is intentionally made to be very high, so that there will be enough dye to make good measurements after the distribution has spread.)

[27] There is a *very* small long-range transport of some tiny droplets that are produced by tip streaming of the oil, but this accounts for less than 1% of the total oil in the system.

[28] Note: we are neglecting inertial effects and Stokes drag in this simplified analysis. A complete analysis will have to account for these effects to verify whether or not small oil droplets truly behave as passive tracers.

[29] Most of this is done automatically, using erosion and dilation techniques to separate the different clusters while maintaining their area. However, it is still necessary to review the images manually and separate some clusters interactively.

FIGURE CAPTIONS

FIG. 1. Velocity field for a two-dimensional flow composed of a chain of alternating vortices, analogous either to Rayleigh-Bénard convection or to the vortex flow studied in these experiments. The equations used to generate this field assume fixed, no-slip boundary conditions at the top and bottom boundaries.

FIG. 2. Diagram of experimental apparatus. (a) Side view. (b) Exploded view of magnetohydrodynamic forcing. A current passing through the thin layer of salt water interacts with an alternating magnetic field to produce a chain of vortices. (c) Exaggerated view of side-walls, emphasizing the double-step tabs used to control the meniscus. The bottom step is 0.20 cm high, and the upper step is 0.05 cm above the bottom step. The fluid is almost perfectly horizontal in the region of interest.

FIG. 3. Sequence of images showing transport of uranine dye (miscible) with oscillation amplitude $b = 0.12$; time (from the top): 0 s, 18 s, 39 s, 75 s and 189 s, corresponding to 0, 1, 2, 4 and 10 periods of oscillation.

FIG. 4. Smoothed concentration profiles (dotted lines) with Gaussian fits (solid lines) for sequence shown in Fig. 3; miscible impurity, $b = 0.12$; times 0 s (narrow curve), 600 s (medium), and 1200 s (broad).

FIG. 5. Variance $\langle x^2(t) \rangle$ for transport of miscible impurities; $b = 0.06$ (triangles, lower curve), 0.12 (circles, middle curve), and 0.24 (squares, upper curve). The solid lines show the predicted growth of $\langle x^2(t) \rangle$, based on the size of the lobes (see Ref. 7).

FIG. 6. Sequence of images showing transport of oil (immiscible) with $b = 0.12$. (a) Small resiliency; $\tau = 3.0$ s. (b) Medium resiliency; $\tau = 1.5$ s. (c) Large resiliency; $\tau = 0.5$ s. For each case, the time (from the top) is: 18 s, 39 s, 75 s, 189 s, and 1890 s, corresponding to 1, 2, 4, 10, and 99 periods of oscillation.

FIG. 7. Smoothed concentration profiles (dotted lines) with Gaussian fits (solid lines) for sequence shown in Fig. 6a; immiscible impurity, $b = 0.12$, resiliency $\tau = 3.0$ s. Time: 0 s (narrow curve), 600 s (medium), and 1200 s (broad curve).

FIG. 8. Variance $\langle x^2(t)\rangle$ for sequences in Figs. 6a and b. The squares correspond to the small resiliency ($\tau = 3.0$ s) case, shown in Fig. 6a. The triangles correspond to the medium resiliency case ($\tau = 1.5$ s), shown in Fig. 6b. The variance $\langle x^2(t)\rangle$ for miscible transport under the same conditions is shown as the top solid curve for reference.

FIG. 9. Drop size analysis for immiscible transport run of Fig. 6a; $b = 0.12$, $\tau = 3.0$ s. The non-dimensional droplet area is $\Gamma = A/l$, where A and l are the droplet and lobe areas, respectively. The fraction distribution f represents the fraction of all the oil in the system contained in droplets with non-dimensional area less than Γ. The four curves correspond to (from the bottom): 30 s, 60 s, 120 s and 1500 s after initiation of the oscillation.

FIG. 10. Characteristic non-dimensional droplet area $\Gamma_c(t)$ for immiscible experiments from Fig. 6; $b = 0.12$. (a) Runs from Figs. 6a and b, corresponding to $\tau = 3.0$ s (bottom, solid curve) and 1.5 s (upper, dotted curve). (b) Run from Fig. 6c, with τ =0.5 s.

FIG. 11. Sequence of images showing transport of oil (immiscible) with $b = 0.24$. (a) Small resiliency; $\tau = 3.0$ s. (b) Large resiliency; $\tau = 0.5$ s. For each case, the time (from the top) is: 18 s, 39 s, 75 s, 189 s, and 1890 s, corresponding to

FIG. 12. Analysis of data from experiments shown in Fig. 11; $b = 0.24$. (a) Characteristic non-dimensional droplet area $\Gamma_c(t)$; $\tau = 3.0$ s (solid, lower curve); $\tau = 0.5$ s (dotted, upper curve). (b) Variance $\langle x^2(t)\rangle$; $\tau = 3.0$ s (triangles, upper curve); $\tau = 0.5$ s (circles, lower curve). The data from the run with miscible dye is also included on this graph for reference (upper solid curve).

FIG. 13. Immiscible transport, $b = 0.06$, small droplet resiliency ($\tau = 3.0$ s). (a) Sequence of images, corresponding to (from top): 18 s, 39 s, 75 s, 189 s and 1889 s (1, 2, 4, 10 and 99 periods of oscillation, respectively). (b) Variance $\langle x^2(t)\rangle$ (circles), along with results from miscible case (solid curve). (c) Characteristic droplet size $\Gamma_c(t)$.

FIG. 14. Immiscible transport with oil artificially broken up; $b = 0.06$, $\tau = 3.0$ s. (a) Sequence of images, corresponding to (from top): 18 s, 39 s, 75 s, 189 s and 1903 s (1, 2, 4, 10 and 100 periods of oscillation). (b) Variance $\langle x^2(t)\rangle$ (circles), along with results from miscible case (solid curve).

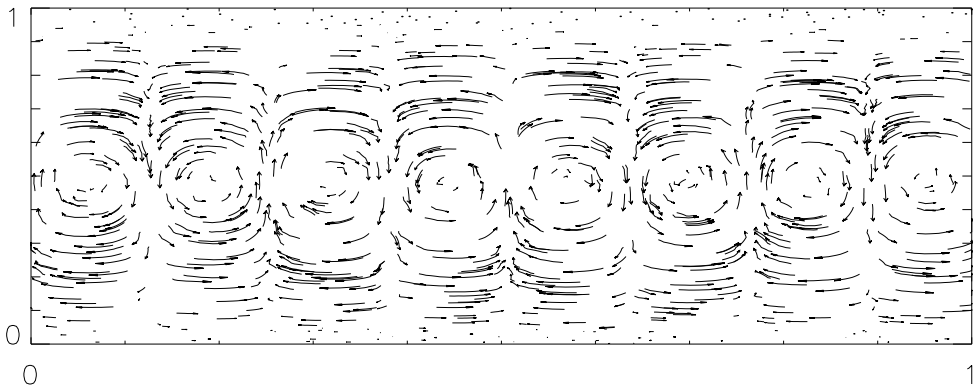

FIG. 1. Velocity field for a two-dimensional flow composed of a chain of alternating vortices, analogous either to Rayleigh-Bénard convection or to the vortex flow studied in these experiments. The equations used to generate this field assume fixed, no-slip boundary conditions at the top and bottom boundaries.

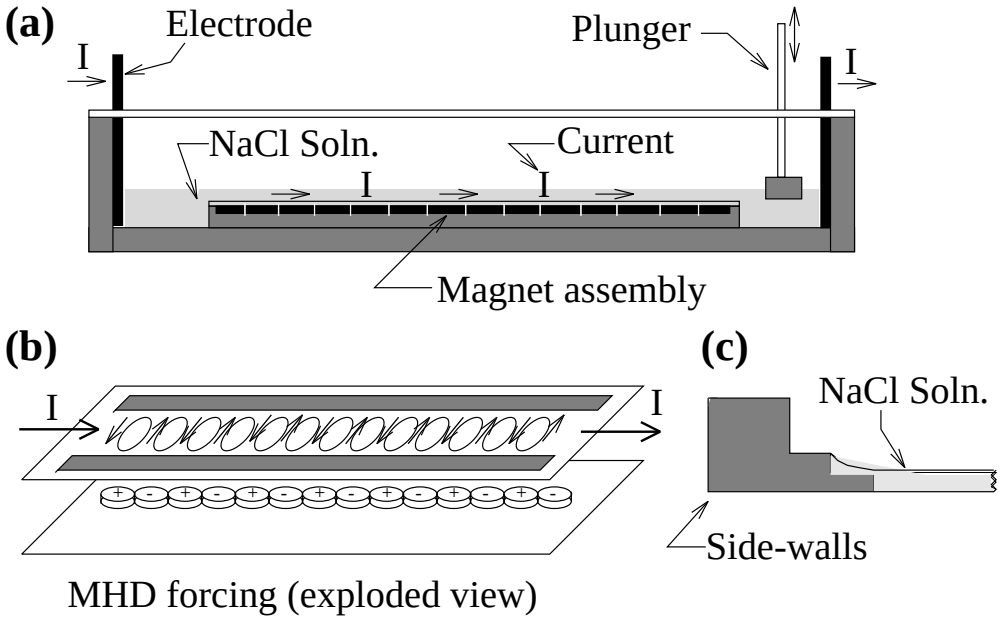

FIG. 2. Diagram of experimental apparatus. (a) Side view. (b) Exploded view of magneto-hydrodynamic forcing. A current passing through the thin layer of salt water interacts with an alternating magnetic field to produce a chain of vortices. (c) Exaggerated view of side-walls, emphasizing the double-step tabs used to control the meniscus. The bottom step is 0.20 cm high, and the upper step is 0.05 cm above the bottom step. The fluid is almost perfectly horizontal in the region of interest.

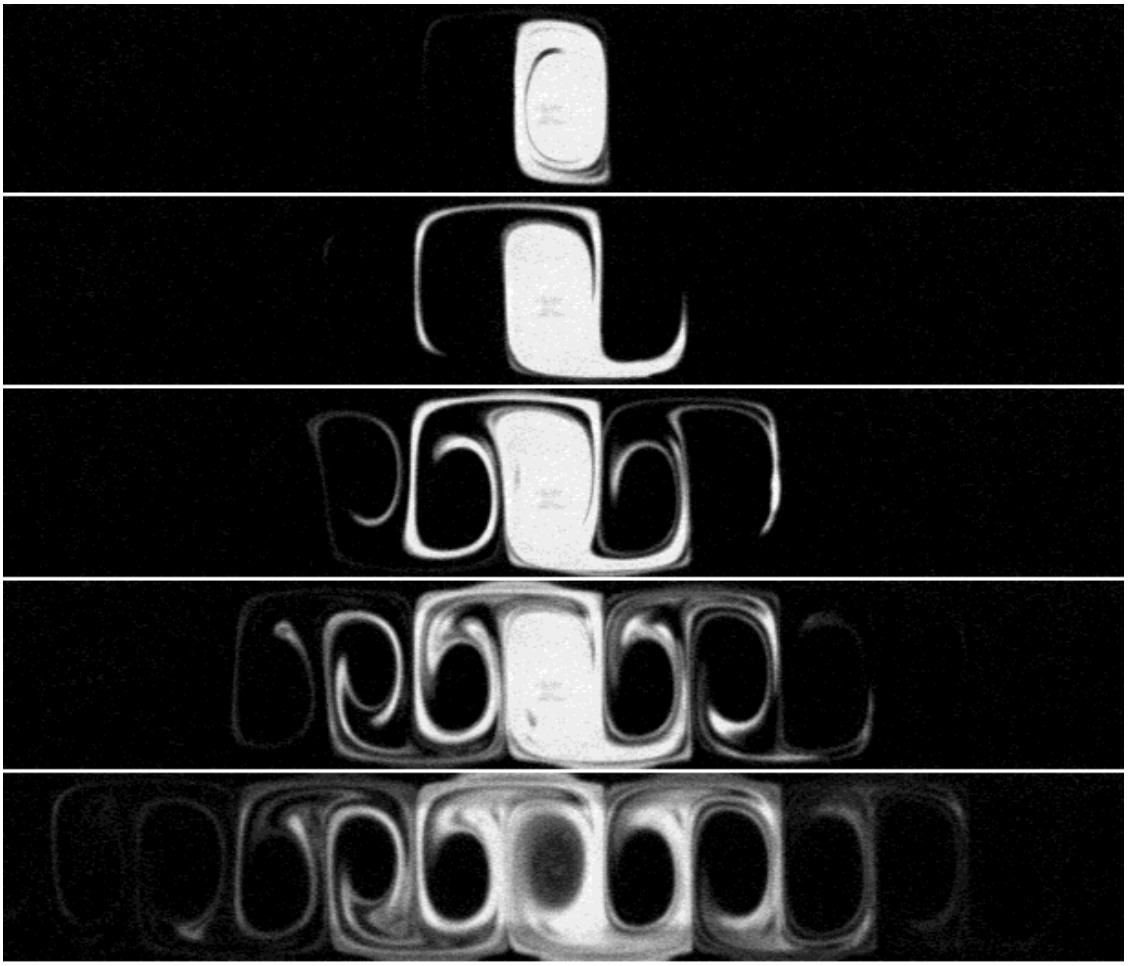

FIG. 3. Sequence of images showing transport of uranine dye (miscible) with oscillation amplitude $b = 0.12$; time (from the top): 0 s, 18 s, 39 s, 75 s and 189 s, corresponding to 0, 1, 2, 4 and 10 periods of oscillation.

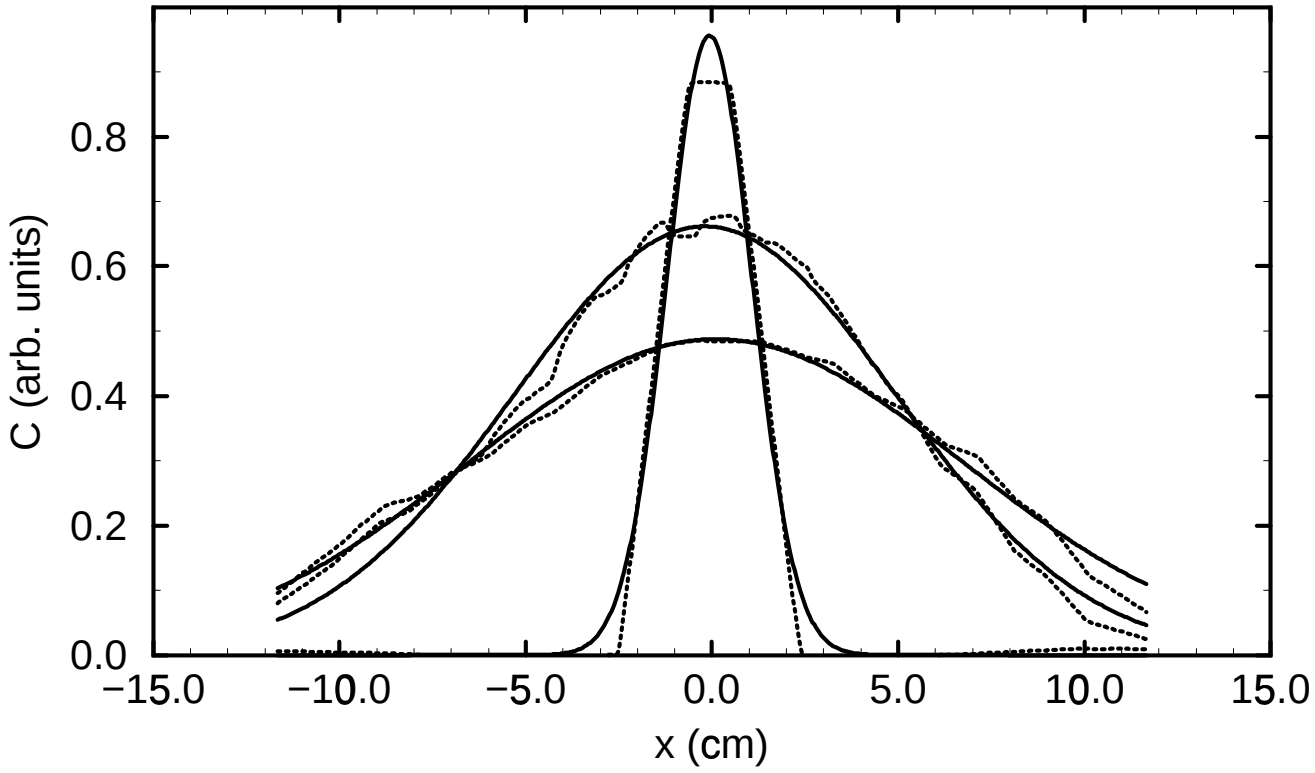

FIG. 4. Smoothed concentration profiles (dotted lines) with Gaussian fits (solid lines) for sequence shown in Fig. 3; miscible impurity, $b = 0.12$; times 0 s (narrow curve), 600 s (medium), and 1200 s (broad).

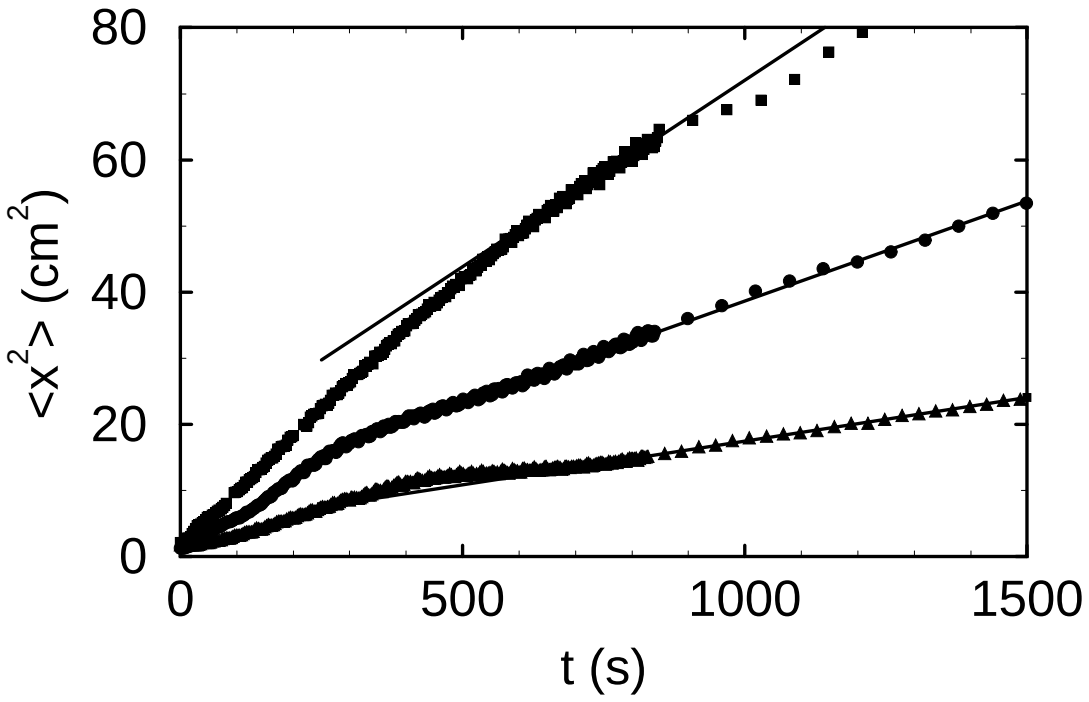

FIG. 5. Variance $\langle x^2(t)\rangle$ for transport of miscible impurities; $b = 0.06$ (triangles, lower curve), 0.12 (circles, middle curve), and 0.24 (squares, upper curve). The solid lines show the predicted growth of $\langle x^2(t)\rangle$, based on the size of the lobes (see Ref. 7).

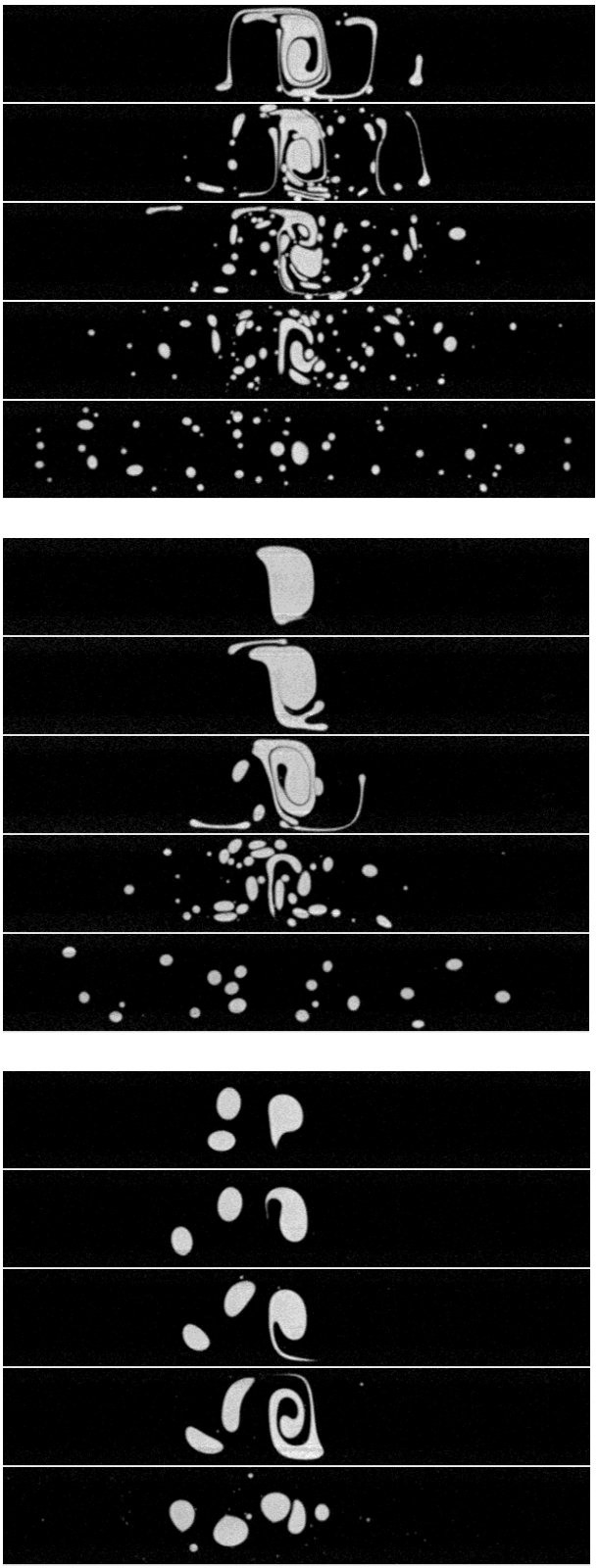

FIG. 6. Sequence of images showing transport of oil (immiscible) with $b = 0.12$. (a) Small resiliency; $\tau = 3.0$ s. (b) Medium resiliency; $\tau = 1.5$ s. (c) Large resiliency; $\tau = 0.5$ s. For each case, the time (from the top) is: 18 s, 39 s, 75 s, 189 s, and 1890 s, corresponding to 1, 2, 4, 10, and 99 periods of oscillation.

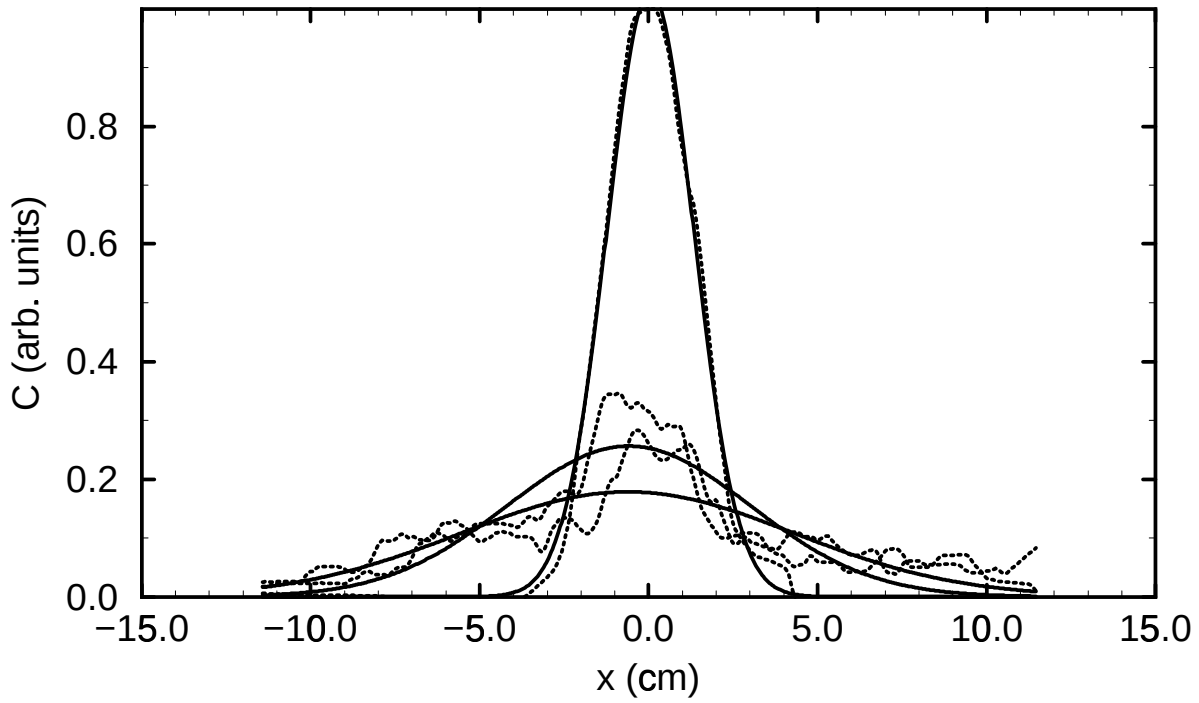

FIG. 7. Smoothed concentration profiles (dotted lines) with Gaussian fits (solid lines) for sequence shown in Fig. 6a; immiscible impurity, $b = 0.12$, resiliency $\tau = 3.0$ s. Time: 0 s (narrow curve), 600 s (medium), and 1200 s (broad curve).

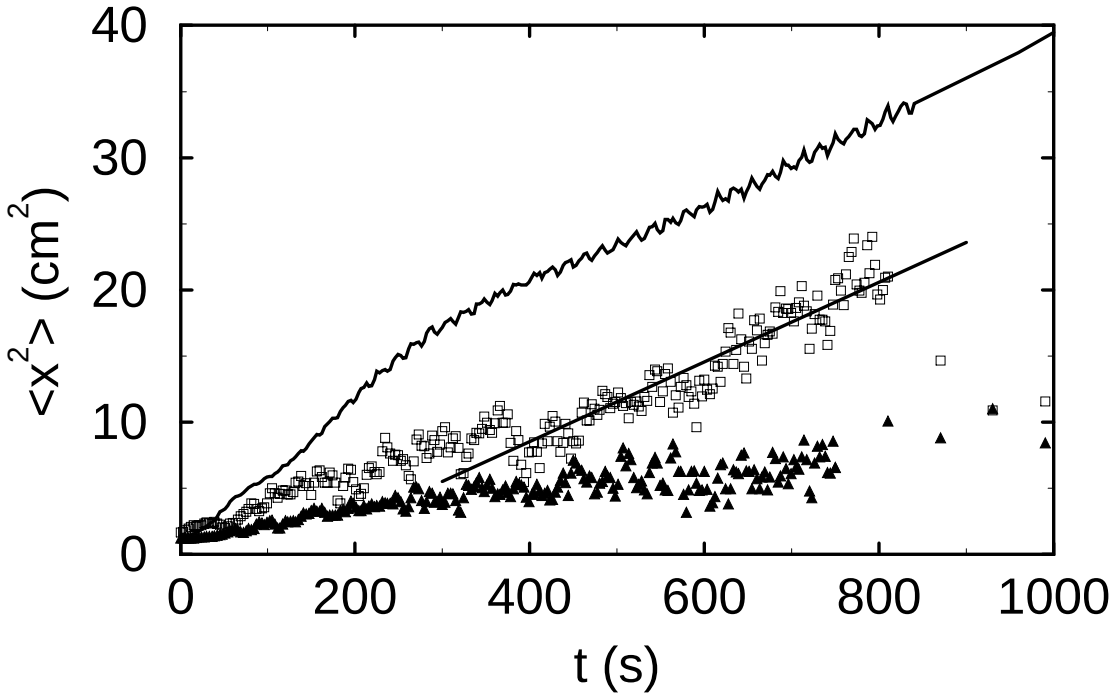

FIG. 8. Variance $\langle x^2(t) \rangle$ for sequences in Figs. 6a and b. The squares correspond to the small resiliency ($\tau = 3.0$ s) case, shown in Fig. 6a. The triangles correspond to the medium resiliency case ($\tau = 1.5$ s), shown in Fig. 6b. The variance $\langle x^2(t) \rangle$ for miscible transport under the same conditions is shown as the top solid curve for reference.

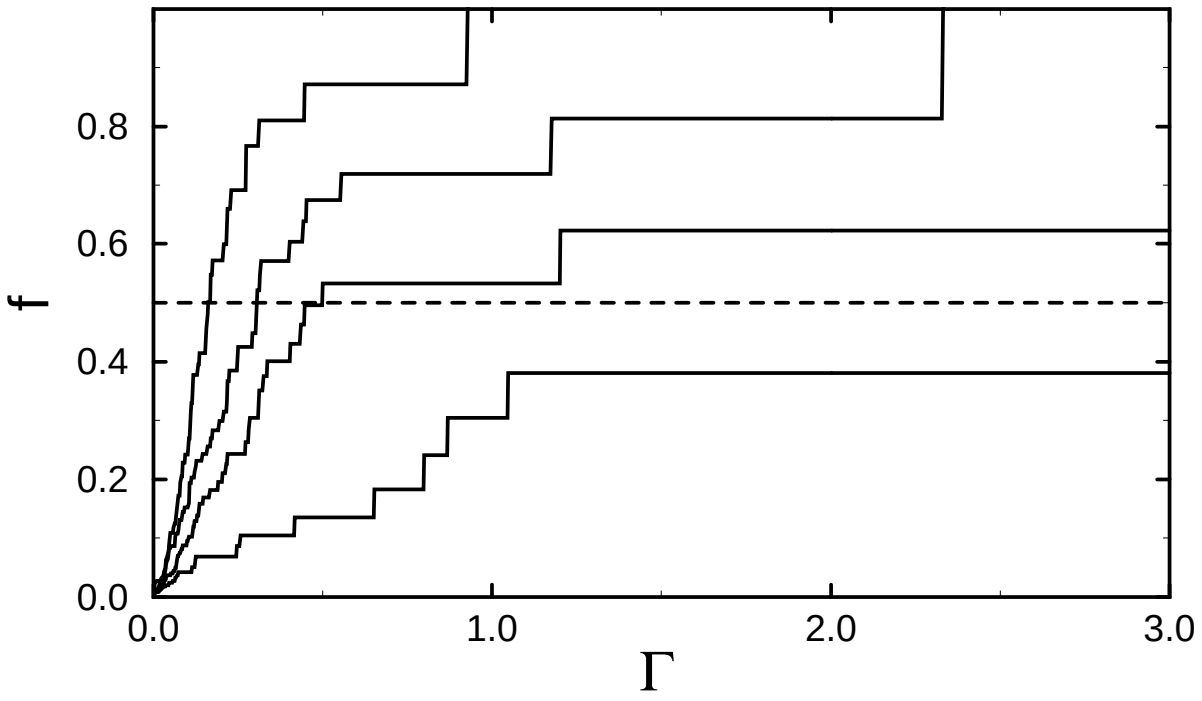

FIG. 9. Drop size analysis for immiscible transport run of Fig. 6a; $b = 0.12$, $\tau = 3.0$ s. The non-dimensional droplet area is $\Gamma = A/l$, where A and l are the droplet and lobe areas, respectively. The fraction distribution f represents the fraction of all the oil in the system contained in droplets with non-dimensional area less than Γ. The four curves correspond to (from the bottom): 30 s, 60 s, 120 s and 1500 s after initiation of the oscillation.

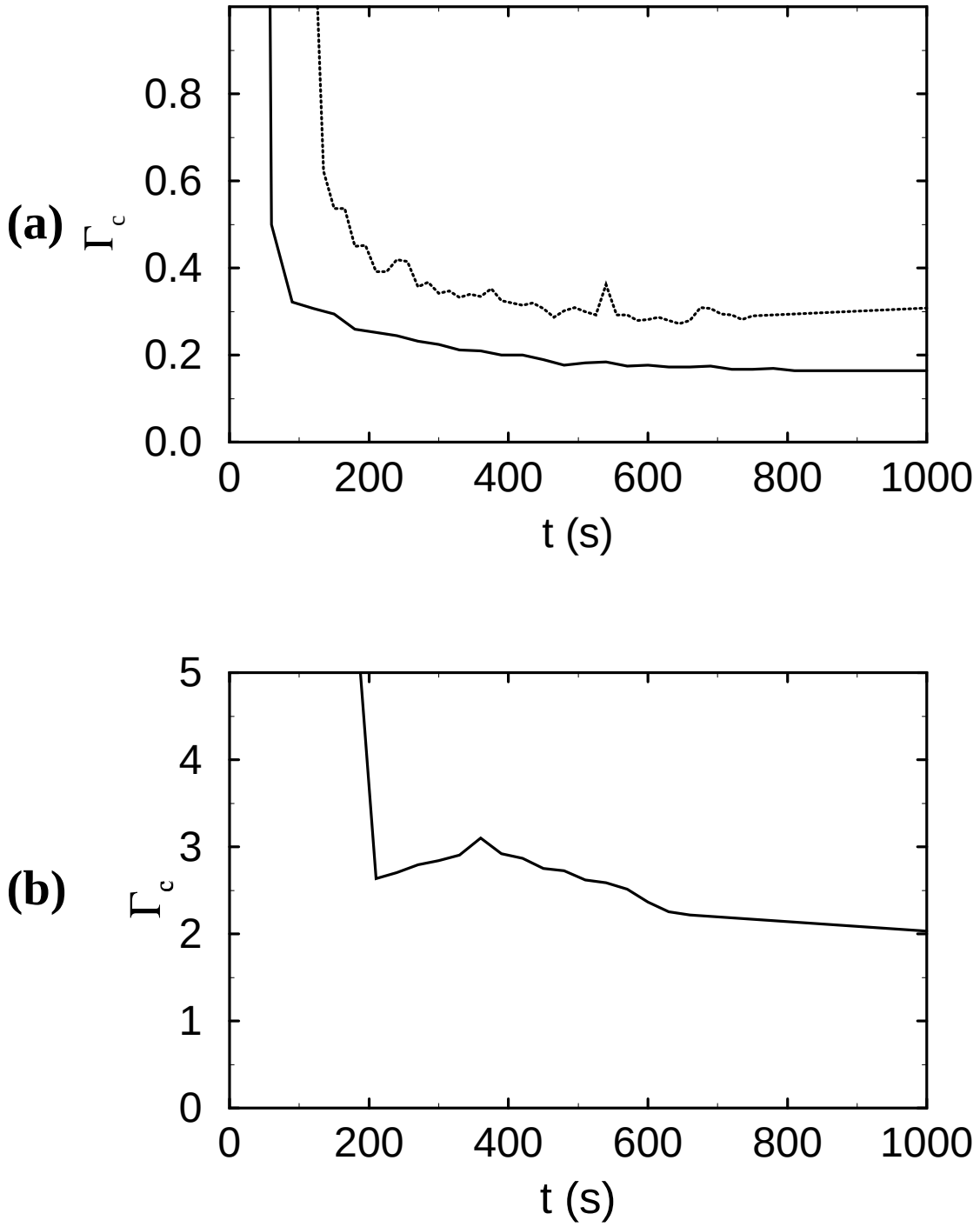

FIG. 10. Characteristic non-dimensional droplet area $\Gamma_c(t)$ for immiscible experiments from Fig. 6; $b = 0.12$. (a) Runs from Figs. 6a and b, corresponding to $\tau = 3.0$ s (bottom, solid curve) and 1.5 s (upper, dotted curve). (b) Run from Fig. 6c, with τ =0.5 s.

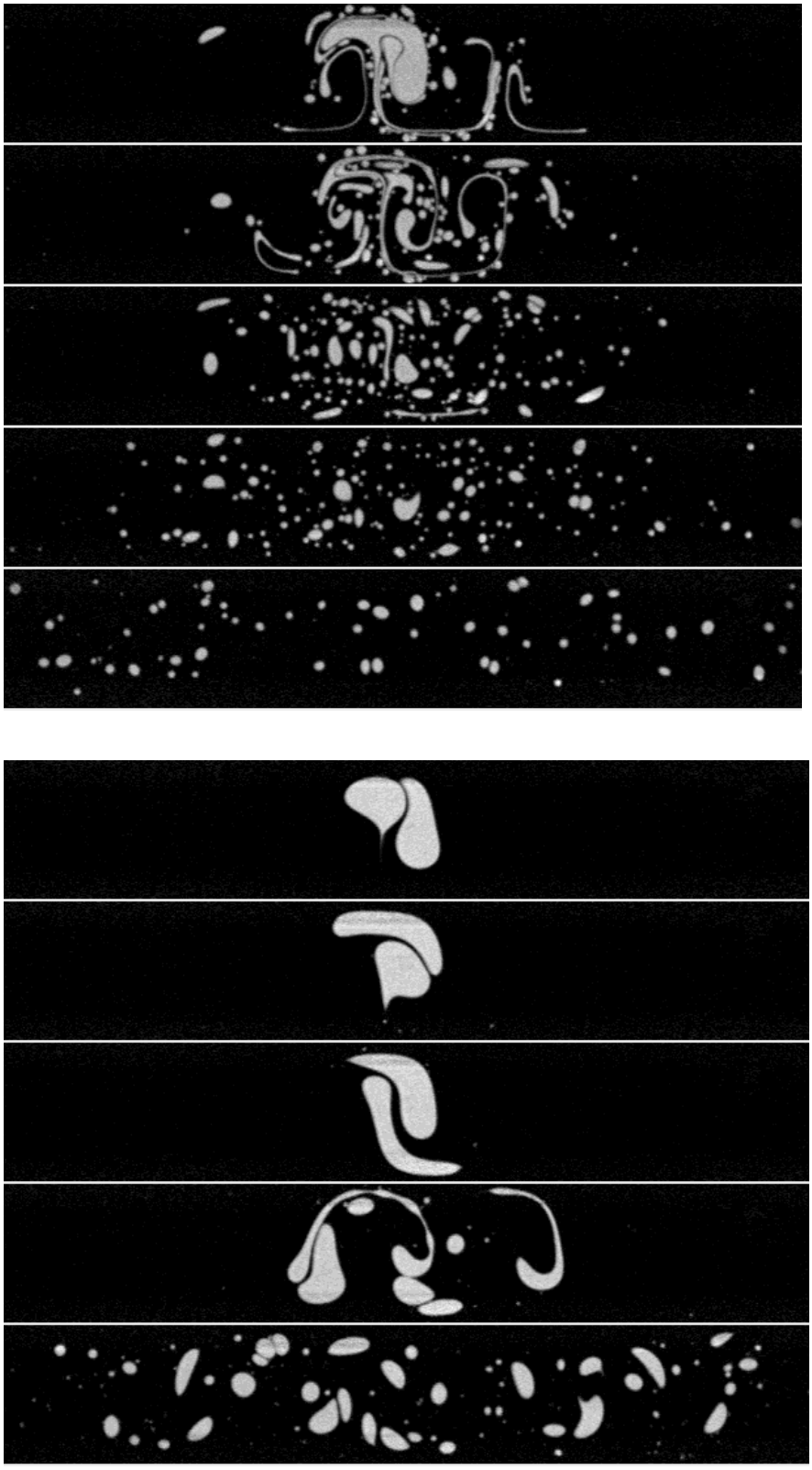

FIG. 11. Sequence of images showing transport of oil (immiscible) with $b = 0.24$. (a) Small resiliency; $\tau = 3.0$ s. (b) Large resiliency; $\tau = 0.5$ s. For each case, the time (from the top) is: 18 s, 39 s, 75 s, 189 s, and 1890 s, corresponding to 1, 2, 4, 10, and 99 periods of oscillation.

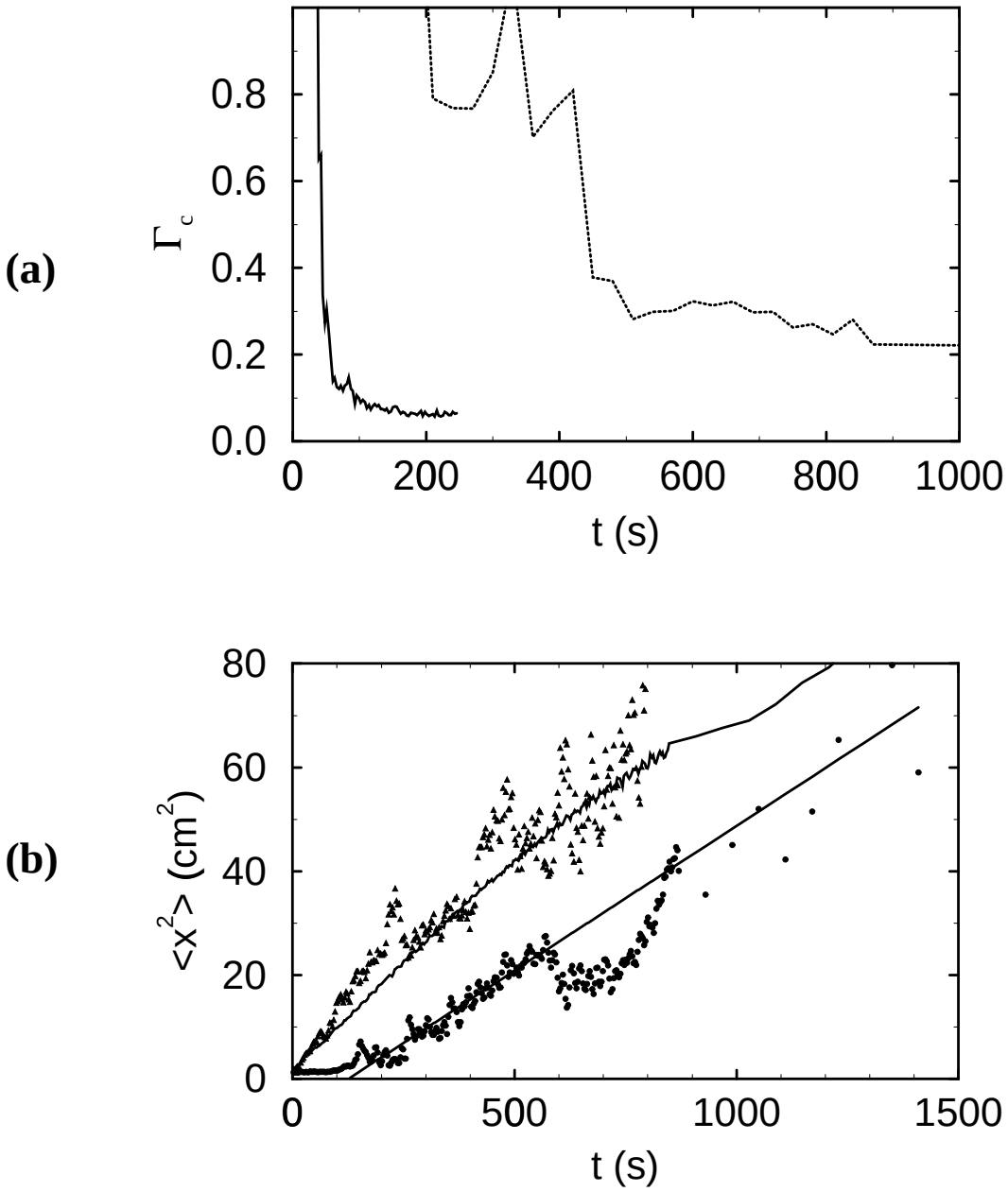

FIG. 12. Analysis of data from experiments shown in Fig. 11; $b = 0.24$. (a) Characteristic non-dimensional droplet area $\Gamma_c(t)$; $\tau = 3.0$ s (solid, lower curve); $\tau = 0.5$ s (dotted, upper curve). (b) Variance $\langle x^2(t) \rangle$; $\tau = 3.0$ s (triangles, upper curve); $\tau = 0.5$ s (circles, lower curve). The data from the run with miscible dye is also included on this graph for reference (upper solid curve).

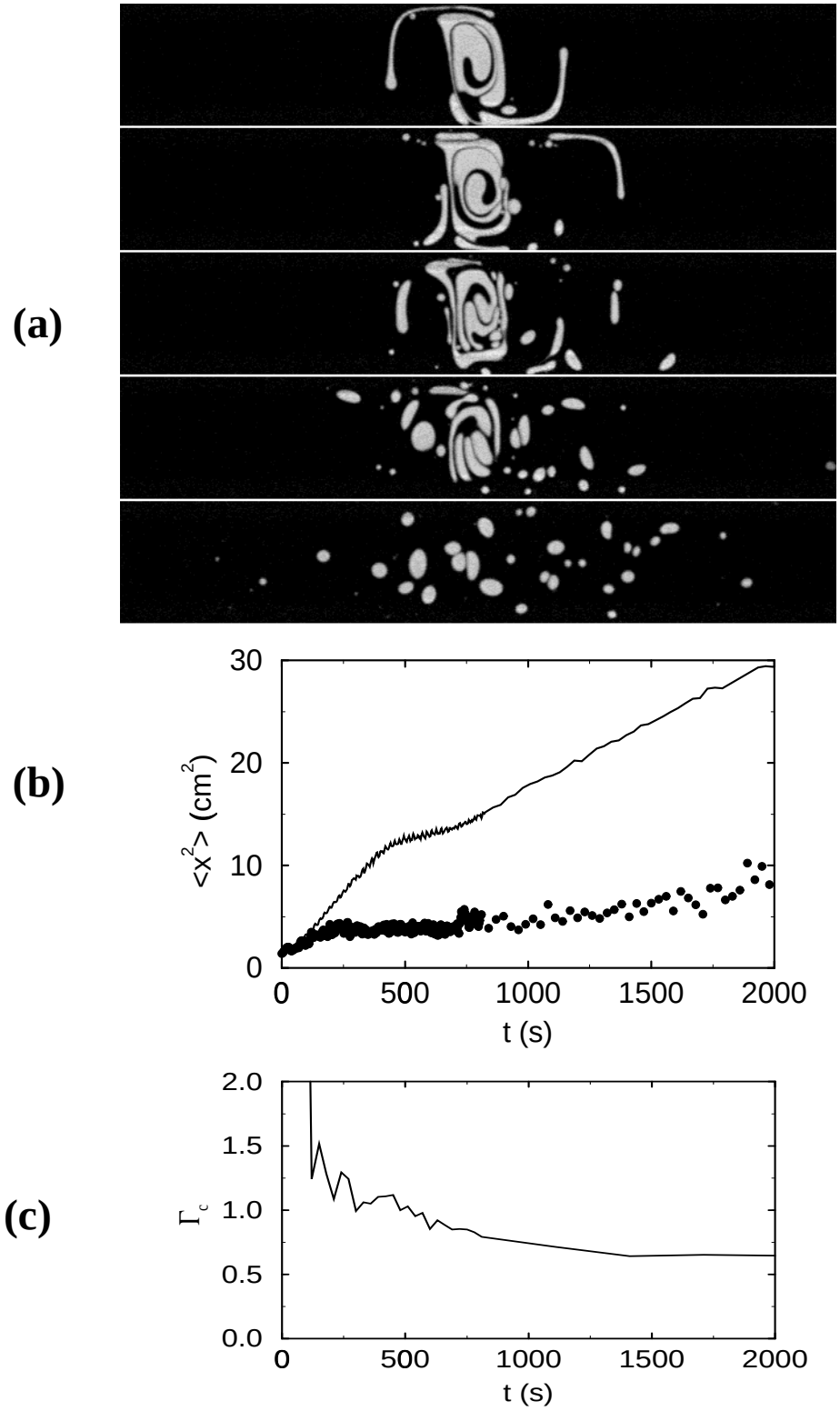

FIG. 13. Immiscible transport, $b = 0.06$, small droplet resiliency ($\tau = 3.0$ s). (a) Sequence of images, corresponding to (from top): 18 s, 39 s, 75 s, 189 s and 1889 s (1, 2, 4, 10 and 99 periods of oscillation, respectively). (b) Variance $\langle x^2(t) \rangle$ (circles), along with results from miscible case (solid curve). (c) Characteristic droplet size $\Gamma_c(t)$.

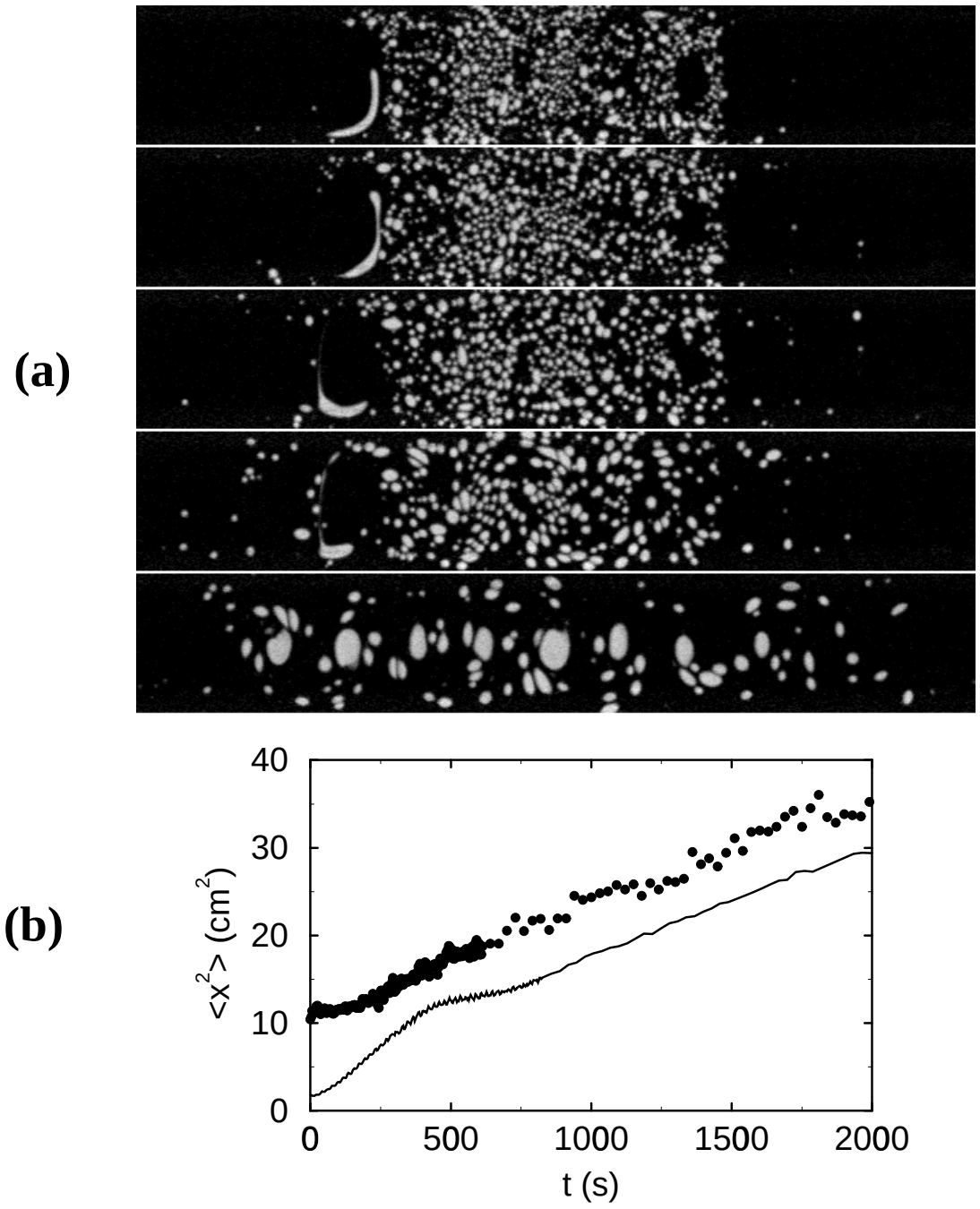

FIG. 14. Immiscible transport with oil artificially broken up; $b = 0.06$, $\tau = 3.0$ s. (a) Sequence of images, corresponding to (from top): 18 s, 39 s, 75 s, 189 s and 1903 s (1, 2, 4, 10 and 100 periods of oscillation). (b) Variance $\langle x^2(t) \rangle$ (circles), along with results from miscible case (solid curve).